AGU PUBLICATIONS

JGR

Journal of Geophysical Research: Solid Earth

RESEARCH ARTICLE
10.1002/2017JB014529

Key Points:
- Two transient events in loading displacements are detected by applying multichannel singular spectral analysis to GPS and GRACE data
- The transient signals agree well with the modeled displacements due to changes in surface mass balance (SMB) and glacial dynamics
- The 2008-2011 transient was due to both SMB and glacial dynamics; the 2011-2014 transient was mainly due to abnormal SMB

Supporting Information:
- Supporting Information S1

Correspondence to:
L. Liu,
liulin@cuhk.edu.hk

Citation:
Zhang, B., Liu, L., Khan, S. A., van Dam, T., Zhang, E., & Yao, Y. (2017). Transient variations in glacial mass near Upernavik Isstrøm (west Greenland) detected by the combined use of GPS and GRACE data. *Journal of Geophysical Research: Solid Earth*, *122*, 10,626–10,642. https://doi.org/10.1002/2017JB014529

Received 5 JUN 2017
Accepted 17 NOV 2017
Accepted article online 23 NOV 2017
Published online 29 DEC 2017

Transient Variations in Glacial Mass Near Upernavik Isstrøm (West Greenland) Detected by the Combined Use of GPS and GRACE Data

Bao Zhang[1,2], Lin Liu[1], Shfaqat Abbas Khan[3], Tonie van Dam[4], Enze Zhang[1], and Yibin Yao[2]

[1]Earth System Science Programme, Faculty of Science, Chinese University of Hong Kong, Hong Kong, [2]School of Geodesy and Geomatics, Wuhan University, Wuhan, China, [3]Department of Geodesy, DTU Space-National Space Institute, Technical University of Denmark, Kongens Lyngby, Denmark, [4]Faculty of Science, Technology, and Communication, University of Luxembourg, Luxembourg City, Luxembourg

Abstract The continuously operating Global Positioning System (GPS) sites mounted on bedrock around the coast of Greenland provide important geodetic data sets to quantify the solid Earth's response to historical and present-day ice mass variations. However, the presence of colored noise and irregular seasonal signals makes it difficult to detect transient changes in GPS time series. Here we apply the multichannel singular spectral analysis to the combination of GPS data and Gravity Recovery and Climate Experiment (GRACE) data so that we can identify and fully utilize the spatial correlations from these two independent data sets. Using the GPS and GRACE data near Upernavik Isstrøm in West Greenland as an example, we demonstrate that this method successfully detects two transient signals in ice mass variations during 2008 and 2014. Our forward modeling of loading displacements due to changes in surface mass balance (SMB) and ice dynamics suggests that the transient change starting in mid-2008 was due to the combined contributions from dynamically induced mass loss and SMB. The transient change starting in mid-2011 was mainly due to ablation. Specifically, the ice melted more in 2012 and less in 2013 with little contribution from anomalies in accumulation.

1. Introduction

Studies of Greenland ice mass balance are usually framed as long-term changes in surface mass balance (SMB) processes and ice discharge at the grounding line, both of which are controlled by atmospheric and oceanic conditions. None of these fluctuations are truly steady. SMB is the difference between accumulation from precipitation (snow and rain), and mass loss from ablation (melting, sublimation, and runoff). Accumulation and runoff vary strongly during the year and between years, largely driven by changes in weather conditions (Abdalati & Steffen, 2001; Hanna et al., 2011; Steffen & Box, 2001). For instance, an extreme melting event occurred in 2012 when 98% of the Greenland Ice Sheet reached the melting temperature (Tedesco et al., 2013). Increasing observations have demonstrated that many Greenland outlet glaciers can abruptly change their dynamic behavior (Joughin et al., 2004; Moon et al., 2012). Yet few studies focus on detecting and quantifying transient changes in ice mass balance.

In the past decade the Greenland GPS network (GNET), deployed on bedrock around the coast of Greenland, has been continuously operating and monitoring the crustal displacement caused by the solid Earth's elastic/viscoelastic response to present/historical ice mass changes (Adhikari et al., 2017; Bevis et al., 2012; Khan et al., 2014; Khan, Liu, et al., 2010; Khan et al., 2016; Khan, Wahr, et al., 2010; Liu et al., 2017). Most of the previous studies have been focusing on the linear and seasonal changes in crustal loading/unloading, whereas only a few investigated short-term changes. Bevis et al. (2012) and Nielsen et al. (2012) found anomalies in crustal uplift at GNET sites by examining the deviation of the GPS time series from a best fit linear plus seasonal model. However, their seasonal model employed constant phase and amplitude, which deviates from the fact that both the phase and amplitude of the seasonal signals vary with time. Such simplification may limit the robustness and accuracy for detecting transient changes. If we cannot reasonably define and extract seasonal and transient signals, we cannot also accurately estimate the linear trend, especially when the time series is short. Moreover, the GPS data used by Bevis et al. (2012) and Nielsen et al. (2012) only spanned the period from 2007 to 2011, which was insufficient to

reveal the complete process of anomalies that initiated in mid-2010 and later. Transient variations in glacial mass have not yet been quantified or investigated in detail, which limits our understanding of short-term (interannual or shorter) variations in glacial mass. These limitations motivate us to introduce an improved method and use multisources of data sets to detect and study the transient variations in glacial mass.

In this study, we combine GPS and Gravity Recovery and Climate Experiment (GRACE) data sets to reliably detect and quantify the transient variations in ice mass change and further investigate the contributors for these variations through forward modeling. Specifically, we use advanced signal analysis techniques, centered around multichannel singular spectral analysis (M-SSA), to separate transient signals from the seasonal and noise components in the geodetic time series. Furthermore, using independent data sets from climate model outputs and glacial velocity measurements, we separately model the vertical loading displacements due to SMB and glacial dynamics. Our forward modeling provides quantitative insights on the relative contributions from these two mechanisms to the detected transient signals.

In this paper, we first briefly review the commonly used transient detection methods (section 2.1) and the M-SSA method (section 2.2). In sections 3 and 4, the GPS and GRACE data analysis are described, respectively. Then M-SSA is applied to (1) the vertical GPS time series from two sites near Upernavik Isstrøm (section 5.1) and (2) the combination of GPS and GRACE data (section 5.2). We demonstrate how to combine GPS and GRACE data to perform the M-SSA, which detects two transient signals that pass the statistical significance test. To investigate the geophysical mechanisms for the detected transient signals, we analyzed the SMB data (section 6.1) and fluctuations in ice discharge (section 6.2). In section 7, we discuss the geophysical reasons for the detected transient signals.

2. Singular Spectrum Analysis

2.1. Review of Transient Detection Methods Applied to Geodetic Data

McGuire and Segall (2003) used the Heaviside function, Green's functions and reference frame errors, random walk noise, and white noise to describe the time-varying GPS site positions. They resolved transient aseismic fault slip using an extended Kalman filter algorithm with spatial and temporal smoothing parameters. Ohtani et al. (2010) developed a Network Strain Filter (NSF) to detect transient deformation signals from large-scale GPS arrays. In addition to the secular motion, benchmark motion, reference frame errors, and white noise, the NSF used a spatial wavelet basis with temporally varying coefficients to represent transient displacements. All these parameters together with smoothing parameters are estimated by a Kalman filter. Ji and Herring (2013) proposed a method based on Kalman filter and principal component analysis (PCA) to detect transient signals. In this method, the linear and seasonal signals are regarded as deterministic, while the noise and transient signals are treated as stochastic, the latter of which is described by a first-order Gauss-Markov (FOGM) process. By running a Kalman smoother, the signal-to-noise ratio (SNR) in time is improved, and the FOGM estimates can account for the transient signals and colored noise. Then PCA is applied to FOGM estimates to improve SNR in space. By checking PCA uncertainties in space and time, the transient signals can be identified. This method provides the key ideas and steps of detecting transient signals: the first is to increase SNR in space and time, and the second is to use the spatial coherence to separate transient signals from colored noise. However, the functional model of the Kalman filter method uses constant velocities, amplitudes, and phases, therefore cannot fully describe the real cases when the velocities of the linear signal and the amplitudes and phases of the seasonal signals change with time. This drawback may lead to misidentifying signals. Riel et al. (2014) proposed a sparse estimation technique to detect transient signals. This method uses a predefined dictionary of displacement functions in time to describe transient signals at various timescales. By introducing a regularization term, the sparse functions can be solved by a least squares estimation.

Singular spectrum analysis (SSA) is designed to extract information from noisy time series and has been proven an effective way to extract seasonal signals from a single GPS time series (Chen et al., 2013; Ghil et al., 2002). Its multivariate form multichannel SSA (M-SSA) is more effective for handling multiple data sets and has been successfully applied to extract periodic and nonperiodic variations from GRACE (Rangelova et al., 2012, 2010) and GPS data (Walwer et al., 2016).

2.2. Multichannel SSA

M-SSA is an advanced data-adaptive method that detects various signals based on simultaneously taking advantage of the spatial and temporal correlations in geophysical fields. It does not require a priori information on function or stochastic model, which makes it flexibly applied to various kinds of data. Based on these advantages, we choose M-SSA to detect and study the transient variations in glacial mass.

We briefly describe the mathematical framework of M-SSA in this section and Monte Carlo SSA in section 2.3. The readers can refer to Ghil et al. (2002) and Walwer et al. (2016) for further details.

Assume

$$\{X_l(n) : l = 1, \ldots, L; n = 1, \ldots, N\} \tag{1}$$

is an ensemble of GPS time series; each time series is a channel. L is the number of time series and N is the number of data points in time series or each channel. M-SSA requires continuous data with a constant sampling interval.

The key idea of M-SSA is to exploit the covariance information contained in a series of lagged copies of all $X_l(n)$ over a sliding M-point window (Broomhead & King, 1986; Ghil et al., 2002; Walwer et al., 2016), which can be written as

$$\widetilde{\mathbf{D}}_l = \begin{pmatrix} X_l(1) & X_l(2) & \cdots & X_l(M) \\ X_l(2) & X_l(3) & \cdots & X_l(M+1) \\ \vdots & \vdots & \ddots & \vdots \\ X_l(N') & X_l(N'+1) & \cdots & X_l(N) \end{pmatrix} \tag{2}$$

where $N' = N - M + 1$ and M is the length of the window used to embed the original time series. M must be carefully chosen to optimize the quantity of information while maintaining satisfactory statistical confidence (Ghil et al., 2002; Walwer et al., 2016).

The covariance matrix $\mathbf{T}_{l,l'}$ between channels $X_l(n)$ and $X_{l'}(n)$ can be calculated as (Broomhead & King 1986):

$$\mathbf{T}_{l,l'} = \frac{1}{N'} \widetilde{\mathbf{D}}_l^{\mathsf{T}} \widetilde{\mathbf{D}}_{l'} \tag{3}$$

These matrices are the blocks of a grand covariance matrix $\widetilde{\mathbf{T}}$ (size: $L \times M$, $L \times M$)

$$\widetilde{\mathbf{T}} = \begin{pmatrix} \mathbf{T}_{1,1} & \mathbf{T}_{1,2} & \cdots & \mathbf{T}_{1,L} \\ \mathbf{T}_{2,1} & \mathbf{T}_{2,2} & \cdots & \mathbf{T}_{2,L} \\ \vdots & \vdots & \ddots & \vdots \\ \mathbf{T}_{L,1} & \mathbf{T}_{L,2} & \cdots & \mathbf{T}_{L,L} \end{pmatrix} \tag{4}$$

The covariance matrix $\widetilde{\mathbf{T}}$ can also be estimated directly from the data as a Toeplitz matrix with constant diagonals (Vautard & Ghil, 1989; Walwer et al., 2016). In this study, the Broomhead and King (1986) method is preferred.

Then the eigenvalues and eigenvectors of $\widetilde{\mathbf{T}}$ are obtained from

$$\widetilde{\mathbf{T}}\mathbf{E}^k = \lambda^k \mathbf{E}^k \tag{5}$$

where λ^k and $\mathbf{E}^k$ ($k = 1, 2, \ldots, L \times M$) are the kth eigenvalue and the corresponding eigenvector, respectively. Each $\mathbf{E}^k$ can be seen as a succession of L segments $\mathbf{E}_l^k$ of length M. And $\mathbf{E}_l^k$ is associated with the channel $X_l(n)$. The eigenvectors $\mathbf{E}^k$ are called the spatiotemporal empirical orthogonal functions (ST-EOFs).

Using the following equation, one can project the time series $X_l(n)$ onto the ST-EOFs to obtain the corresponding spatiotemporal principal components (ST-PCs), denoted as $A^k(n)$:

$$A^k(n) = \sum_{j=1}^{M} \sum_{l=1}^{L} X_l(n+j-1) E_l^k(j) \; 1 \le n \le N' \tag{6}$$

where k and l correspond to the kth eigenvector and lth channel, respectively.

The ST-PCs and ST-EOFs allow us to partially reconstruct the time series $X_l(n)$ (Ghil & Vautard, 1991; Vautard et al., 1992). The partial signal $R_l^k(n)$ reconstructed by $\mathbf{A}^k$ and $\mathbf{E}_l^k$ is given by

$$R_l^k(n) = \begin{cases} \frac{1}{n}\sum_{j=1}^{n} A^k(n-j+1)E_l^k(j) & 1 \le n \le M-1 \\ \frac{1}{M}\sum_{j=1}^{M} A^k(n-j+1)E_l^k(j) & M \le n \le N' \\ \frac{1}{N-n+1}\sum_{j=n-N+M}^{M} A^k(n-j+1)E_l^k(j) & N'+1 \le n \le N \end{cases} \quad (7)$$

The partial reconstructions are essentially a filtered time series that may help us to isolate signals of different frequencies that are mixed in the original time series.

2.3. Monte Carlo SSA

Colored noise in GPS time series may have similar temporal behavior as transient signals, thus can be mistaken as signals (Allen & Smith, 1994). So appropriate statistical significance tests are necessary and important to distinguish the signal from noise. Allen and Smith (1996) first proposed the Monte Carlo SSA (MC-SSA) to test the significance of the modes detected by univariate SSA, which was then extended by Allen and Robertson (1996) to the multivariate case. Geophysical signals can be distinguished from colored noise by checking their spatial correlations. But MC-SSA is still useful, especially when the common signals are weak or only a few sites are available, such as our case (only two GPS sites).

The main idea of MC-SSA is to compare whether the partial variance of the data and the surrogate data are statistically different. Surrogate data can be constructed according to particular stochastic models (Theiler et al., 1992). For instance, we can use the power law noise model to generate surrogate data since the power law noise is the canonical noise in GPS time series. Using the power law noise model, we generate surrogate data $\mathbf{X}_R$ of the same length N and dimension L as the data set being analyzed and then compare their partial variances.

The partial variances $\mathbf{\Lambda}_R$ of the surrogate data are calculated by projecting the surrogate data covariance matrix $\widetilde{\mathbf{T}}_R$ to the data ST-EOFs' directions:

$$\mathbf{\Lambda}_R = \mathbf{E}^T \widetilde{\mathbf{T}}_R \mathbf{E} \quad (8)$$

$\widetilde{\mathbf{T}}_R$ is calculated by the same way as $\widetilde{\mathbf{T}}$ in equation (4), but using the ensemble of surrogate data $\mathbf{X}_R$, $\mathbf{E}$ is the matrix whose $L \times M$ columns are the ST-EOFs $\mathbf{E}^k$. Using a sufficiently large number of realizations of the surrogate data, we can calculate an assemble of $\mathbf{\Lambda}_R$ and thus estimate the confidence intervals for the diagonal elements of $\mathbf{\Lambda}_R$. If the eigenvalues of the data covariance matrix are within these confidence intervals, the corresponding components are statistically indistinguishable from the surrogates.

3. Study Area and GPS Data Analysis

3.1. Upernavik Isstrøm and Nearby GPS Sites

Upernavik Isstrøm (UI) consists of five glaciers, denoted as UI 0–4 proceeding from north to south, all terminating into the same fjord (Figure 1a). Nielsen et al. (2012) and Khan et al. (2013) studied the long-linear ice mass change in UI and estimated that the ice mass loss rate of the UI catchment was 6.7 Gt/yr during 2005–2010, of which dynamical mass loss accounts for 80% and SMB accounts for the other 20%. The mass loss rate started to increase in summer 2010 (Nielsen et al., 2012), but this transient change has not been well studied. Previous studies also found asynchronous dynamical changes in the glaciers: UI-1 exhibits significant retreat and speedup since 2006, while the other glaciers showed different changes during the same period (Andresen et al., 2014; Larsen et al., 2016; Nielsen et al., 2012).

Two GPS sites (SRMP and UPVK) are mounted on bedrock near UI (Figure 1a) to measure the gradient in uplift due to nearby ice loss. SRMP (54.3937°W, 72.9107°N) is located only 1.5 km west of the UI-2's frontal position in 2011, whereas UPVK (56.1280°W, 72.7883°N) is on an island located 65 km farther west of the glaciers. To

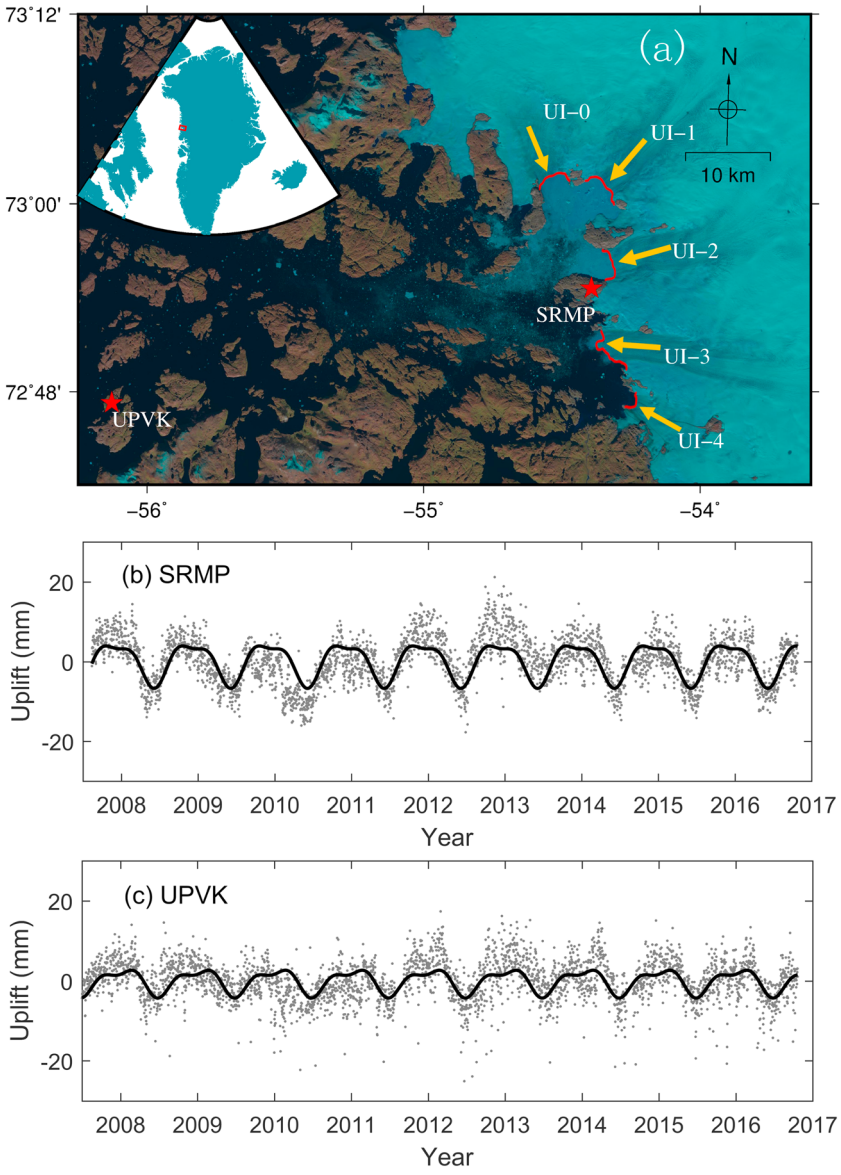

Figure 1. (a) Locations of two GPS sites (red stars) and the five glaciers of Upernavik Isstrøm (labeled as "UI-0" to "UI-4"). The yellow arrows indicate the flow lines of the ice. The red lines indicate the calving front on 28 August 2014. The inset shows the study area in West Greenland. (b and c) Time series of detrended GPS vertical positions (gray dots) and best fit annual plus semiannual terms (black lines) at SRMP and UPVK, respectively. To simplify the figures, uncertainties of the GPS vertical positions are not shown.

obtain daily positions, we process the GPS data from 2007 to 2016 using the GIPSY-OASIS v6.4 software package and using conventional methods detailed in Khan, Liu, et al. (2010) and Liu et al. (2017). We estimate the position uncertainties using the flicker plus white noise model (Khan, Liu, et al. (2010); Williams et al., 2004). We obtain the daily positions and their uncertainties in the local north, east, and up directions in the IGS08 frame (Altamimi et al., 2012) (the GPS time series are maintained by the Technical University of Denmark and available at ftp://ftp.spacecenter.dk/pub/abbas/GNET/v1/). The time series of detrended GPS vertical positions and best fit annual plus semiannual terms are shown in Figure 1b (for SRMP) and Figure 1c (for UPVK).

In this study, we do not investigate the horizontal displacements due to their small magnitudes and azimuthal sensitivity to the nearby glacial mass changes. The horizontal loading displacements are usually 2–3 times smaller in magnitude than the vertical displacements for a single isolated point load, and it will

be much smaller for other cases (Wahr et al., 2013). Because there are five glaciers located near the GPS sites, the horizontal loading displacements caused by each glacier partly cancel out (Wahr et al., 2013). This canceling effect is particularly strong in the north components because ice mass changes occurred on both the north and south sides of the GPS sites. We leave the interpretation of transient changes in horizontal displacements to a future investigation.

3.2. Surface Mass Loadings

The variation of GPS position time series consists of two parts: geophysical signals and noise. Geophysical signals include tectonic movement (such as plate motion) and nontectonic movement, such as movement caused by atmosphere loading (ATML) change (Tregoning & van Dam, 2005), terrestrial water storage (TWS) change (van Dam et al., 2001), ice loading change (Khan, Liu, et al., 2010; Liu et al., 2017), as well as the Earth tides (Penna & Stewart, 2003), ocean tide loading (Melachroinos et al., 2008), and nontidal ocean loading (NTOL) (Williams & Penna, 2011). We fit and remove the linear trend in GPS time series, which effectively removes any secular geophysical contributions (such as glacial isostatic adjustment (GIA) and plate motion) or errors (such as reference frame drift). The annual signal is mainly associated with Earth surface mass change but also slightly influenced by GPS systematic error such as the "GPS draconitic error." As viewed from the Earth, the Sun takes a period of ~351.4 days to return to the same point relative to the GPS orbital nodes. Such periodic variation introduces the GPS draconitic error (Amiri-Simkooei, 2013; Ray et al., 2008). In the GPS data processing, the Earth tides and ocean tidal loading have been corrected for, so the remaining variation in the GPS time series is mainly due to the surface movement caused by the ATML, TWS, NTOL, ice loading, bedrock thermal expansion (Fang et al., 2014), and the draconitic error. The thermal displacement and draconitic error can be eliminated by removing the seasonal signals from the time series and thus will not influence the detection of transient signals. As our purpose is to use GPS to detect transient ice mass change, so the ATML, TWS, and NTOL should be well modeled and removed.

Liu et al. (2017) gave a detailed description of modeling ATML, TWS, and NTOL at the two Upernavik GPS sites. Here we only provide a summary. Given any grid of surface mass changes, we use the elastic loading Green's functions calculated based on the Preliminary Reference Earth Model (PREM) with continental crust to estimate the displacement response at the two GPS sites (Dziewonski & Anderson, 1981). To model the ATML, we use the surface pressure provided by the National Center for Environmental Prediction (NCEP) reanalysis data (Kalnay et al., 1996). We assume the oceans respond to the atmospheric pressure changes as an inverted barometer and introduce a globally uniform pressure change at the ocean bottom to conserve ocean mass (van Dam & Wahr, 1987). The global uncertainty of the atmospheric loading calculated by this method is evaluated at ~15% (Petrov & Boy, 2004). To model the NTOL, we use the "Estimating the Circulation and Climate of the Ocean" data set to quantify the noninverted-barometer ocean bottom pressure changes. The version used is Jet Propulsion Laboratory's Kalman filter (kf66b) series, which assimilates altimetric heights, Expendable Bathythermographs profiles, and other in situ ocean data (Fukumori, 2002; Kim et al., 2007). According to our calculations, there is at least 98% chance that the displacements caused by NTOL at SRMP and UPVK are less than 2 mm, indicating the limited influence of NTOL on the GPS time series. To model the TWS loading, we use the Noah land hydrology model in the Global Land Data Assimilation System (GLDAS) to quantify continental water mass changes at monthly intervals (Rodell et al., 2004, obtained from http://grace.jpl.nasa.gov). The global 1° by 1° product provides a sum of water stored as soil moisture, snow, and canopy, but not including groundwater or the water storage changes in rivers or lakes. It also excludes water storage estimates from the Greenland Ice Sheet and permafrost areas. Our calculated TWS loading displacements at SRMP and UPVK are dominantly regular seasonal changes with magnitudes less than 2 mm, which indicates their minor influence in our investigation on transient changes.

3.3. GPS Noise Analysis

After the ATML, TWS, and NTOL loadings and linear trend are removed, the variations in GPS time series are mainly driven by ice mass change, GPS systematic errors, and noise. A good knowledge of the noise embedded in the data would help us distinguish transient signals resulting from colored noise when the GPS data themselves are insufficient to provide enough spatial correlation. Here the Hector software (Bos et al., 2013) is used to analyze the noise in GPS time series. Before analyzing data, the "SSA-MTM Toolkit" (Ghil et al., 2002) is utilized to interpolate the missing data in daily GPS time series with an iterative SSA method (Kondrashov & Ghil, 2006). Power law noise is the canonical model for noise present in GPS time

Table 1
Spectral Indices and Noise Variance in the Vertical GPS Time Series

	Spectral index	Power law noise (mm/yr$^{1/4}$)	White noise (mm)
SRMP	0.8327	13.44	0.21
UPVK	0.7146	16.27	0.01

Note. The power law noise is scaled to mm/yr$^{1/4}$.

series (Williams, 2003; Williams et al., 2004). The power law process can be expressed in the spectral domain by equation (9).

$$S(f) = S_0\left(\frac{f}{f_0}\right)^{-\alpha} \tag{9}$$

where $S(f)$ is the spectral density, f is the frequency, S_0 and f_0 are constants, and α is the spectral index.

Here we use power law plus white noise as the noise model. The Maximum Likelihood Estimation method is used to estimate functional (linear trend, annual, and semiannual) and stochastic parameters (spectral index and the corresponding noise variance) in Hector. Table 1 lists the spectral indexes and noise variance. Our noise analysis shows that the power law noise is indeed the dominant noise type in our GPS data. To carefully identify transient signals, the estimated parameters in Table 1 will be used later in the MC-SSA test.

4. GRACE Data Analysis

We calculate the vertical displacements due to surface mass loading using the GRACE gravity data. Van Dam et al. (2007) provided a detailed description of this method. The essence of the idea is to convert the time-varying gravitation fields to the radial displacements using the load Love numbers. Here we only provide a summary of this conventional calculation.

The GRACE data we use are the Release-05 Level-2 GSM products from the Center for Space Research (CSR), University of Texas Austin. The CSR GSM products contain spherical harmonic coefficients (i.e., Stokes coefficients) up to degree 60 for each monthly gravity field. We include the degree-1 coefficients calculated by Swenson et al. (2008) and use the monthly degree-2 order-0 coefficients from satellite laser ranging products provided by Cheng et al. (2013). We remove the continental water mass changes from the GLDAS Noah model, which is consistent with our GPS data analysis. The mass contributions from ocean and atmosphere have already been removed from the GRACE GSM products.

We calculate the uplift dr of the Earth's surface at latitude θ and longitude φ using the following equation, same as equation (2) of van Dam et al. (2007):

$$\mathrm{d}r(\theta,\varphi) = R\sum_{l=0}^{l=60}\sum_{m=0}^{m=l} W_l\widetilde{P}_{lm}(\cos\theta)(C_{lm}\cos(m\varphi) + S_{lm}\sin(m\varphi))\frac{h_l^{'}}{1+k_l^{'}} \tag{10}$$

where R is the Earth's radius, l and m are degree and order numbers, $\widetilde{P}_{lm}$ are normalized associated Legendre functions, W_l is the weighting function, $h_l^{'}$ and $k_l^{'}$ are the load Love numbers, and C_{lm} and S_{lm} are the GSM Stokes coefficients. We use the Love numbers provided by Han and Wahr (1995). We apply a Gaussian smoothing kernel of 300 km radius. We do not apply any "destriping" filter as the striping artifacts are negligible over Greenland. We fit and remove a linear trend from the GRACE-based displacement time series. This completely removes the contribution from the GIA. We do not estimate the errors in the GRACE-derived uplifts because these errors are not colored noise and therefore do not affect the MC-SSA test. We refer to the detrended GRACE-derived uplifts as the "GRACE data" hereafter. Both the truncation at degree 60 and the Gaussian smoothing would lead to an attenuation of the GRACE data. We follow Khan, Wahr, et al. (2010) to apply a correction that amplifies the GRACE data to match the GPS data (see section 5.2).

5. Using M-SSA to Detect Transient Changes in GPS and GRACE Time Series

To investigate the potential transient signals in the GPS and GRACE time series, we first apply M-SSA to the GPS data (section 5.1) and then to the combination of GPS and GRACE data (section 5.2).

5.1. Applying M-SSA to GPS Data

GPS vertical position time series from SRMP and UPVK are used to retrieve common modes caused by regional geophysical processes, in this case, ice mass changes near Upernavik Isstrøm. After filling missing data by the SSA-MTM Toolkit, we obtain 3,357 common daily data points from both GPS sites spanning 2,007.6167 to 2,016.8049, which formulate a two-channel SSA. Our synthetic tests in sections S1 and S3 in the supporting information justify our M-SSA settings and suggest that a window width of 700 days could effectively

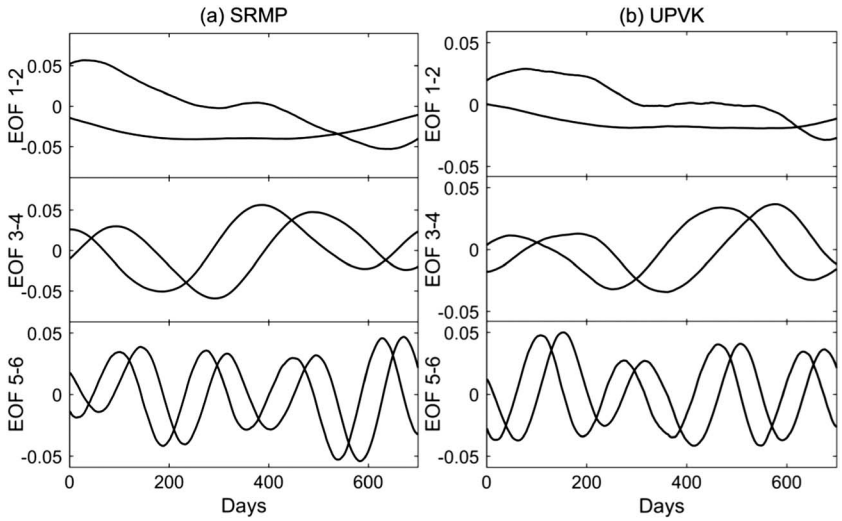

Figure 2. The spatiotemporal empirical orthogonal functions (ST-EOFs) corresponding to the largest six eigenvalues of the M-SSA analysis using GPS vertical time series at SRMP and UPVK.

separate the seasonal and transient signals. After applying M-SSA to the detrended GPS data, we obtain ST-EOFs and partially reconstructed components by using equation (7).

Figure 2 shows the ST-EOFs corresponding to the largest six eigenvalues, including possible transient signals (ST-EOFs 1 and 2), annual signals (ST-EOFs 3 and 4), and semiannual signals (ST-EOFs 5 and 6). Figure 3 shows the first 10 partially reconstructed components (RC), among which the first six correspond to the modes shown in Figure 2. RCs 3 and 4 are mainly annual signals. RCs 5 and 6 are mainly semiannual signals. The amplitudes of the signals are larger at SRMP than at UPVK because SRMP is closer to the ice mass. RCs 7 and 8 appear to be seasonal signals but their varying patterns are not as clear as RCs 3, 4, 5, and 6. From the ninth onward, the RCs are high-frequency signals or noise, which are not of interest to us. Both RCs 1 and 2 indicate strong potential transient signals during 2008 and 2014 (Figure 3). But RC2 is a result of the spectral mixing of the seasonal modes and the transient modes. The sign of spectral mixing is also evident from the eigenvalues in Figure 4. Namely, the second eigenvalue lies between the first and third, rather than coming in pair with the first eigenvalue (two modes with similar variance usually come in pair to represent the same signal, see Rangelova et al., (2010, 2012). Since the number of sites is so small (only two), we cannot rule out the possibility that the colored noise in both time series may show similar variations with transient signals. Therefore, the MC-SSA test is necessary.

In the MC-SSA test, the surrogate data are constructed according to the power law noise model and the parameters in Table 1. Here the first 10 modes are tested by generating surrogate data in the following procedure that is similar to the work of Walwer et al. (2016). We first remove the first 10 RC from the original data. Next, we add the simulated power law noise. Then we apply the MC-SSA to the surrogate data as described in section 2.2 and obtain$\mathbf{\Lambda}_R$ from 500 realizations. Figure 4 shows comparisons among the first 30 eigenvalues and the corresponding 95% confidence intervals from the MC-SSA test.

In Figure 4, from the eleventh eigenvalue onward, the eigenvalues are within the confidence intervals, indicating that these components are within the noise level. Among the first 10 eigenvalues, the first, seventh, and eighth ones are also within the confidence interval, while the others are all above the confidence intervals. Figure 4 shows that the confidence intervals are wide for the transient-associated components (first and second). This is because the Hector software cannot recognize transient signals in the GPS time series but instead treats them as colored noise, thus leading to overestimating the spectral index and variance for the noise. Larger spectral index and noise variance lead to the wider confidence intervals. Therefore, it is possible that a true transient signal might be mistakenly identified as colored noise by the MC-SSA test, especially when the number of sites (i.e., channels) is not sufficient to provide confident common modes in space. Our synthetic tests in section S2 in the supporting information confirm that (1) the transient signals are prone to be misidentified as colored noise and (2) the colored noise with a larger spectral index makes it more difficult

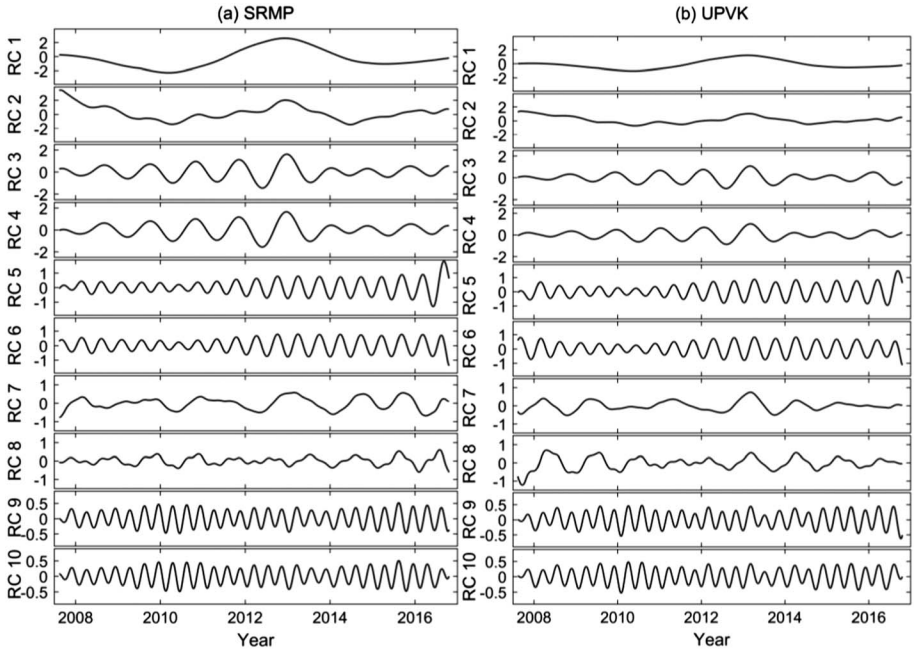

Figure 3. The reconstructed components (RC, in mm) using the first 10 spatiotemporal principal components and ST-EOFs corresponding to the largest 10 eigenvalues.

to accurately detect seasonal and transient signals. In addition, the RC1 in Figure 3 shows very similar variations at both sites which are characteristic of spatially correlated signals other than colored noise. To improve the confidence in identifying transient signals, we combine the GPS and GRACE data to improve the effectiveness of the MC-SSA in distinguishing signals and noise.

5.2. Applying M-SSA to GPS and GRACE Data

Both GRACE and GPS data reflect similar loading signals due to glacial mass changes. Therefore, we can add the GRACE data as the new channel(s) to the two GPS time series in the same M-SSA analysis as the one we apply to the GPS data only in section 5.1. However, the GPS data are daily, whereas the GRACE data are monthly. To make them consistent and applicable in the M-SSA, we interpolate the GRACE data to daily intervals by an iterative form of the SSA method (Kondrashov & Ghil, 2006) provided by the SSA-MTM Toolkit (Dettinger et al., 1995; Ghil et al., 2002). The window width of SSA is 400 days, and the first 40 components are used to reconstruct the GRACE time series. Using this method, we can fully utilize the signals embedded in GRACE monthly data without introducing any artificial components. The interpolated daily data and the original monthly data are shown in Figure 5.

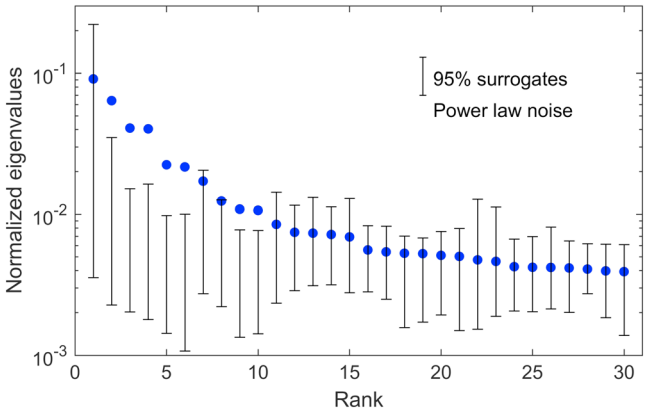

Figure 4. Results of the Monte Carlo SSA tests. The first 10 components are tested against power law noise. Blue dots are the eigenvalues of the covariance matrix of the original time series. The error bars are 95% confidence intervals calculated from 500 realizations of surrogate data.

As the GRACE gravimetric data have a footprint size of ~300 km, much larger than the 60 km distance between SRMP and UPVK, the GRACE-based vertical deformation at the two sites are nearly identical. Therefore, we only use the GRACE-based vertical displacements at SRMP in the remaining analysis and discussion.

We apply the same M-SSA method to the combined GPS (two channels) and GRACE data (one channel). Then we obtain the reconstructed components as shown in Figure 6. The results in Figures 6a and 6b are similar to the previous results using only GPS data shown in Figure 3.

To distinguish the transient signals from noise, we perform the MC-SSA test with the same settings as in section 5.1 to the combination of GPS and GRACE data. Figure 7 shows the test results. Compared with the

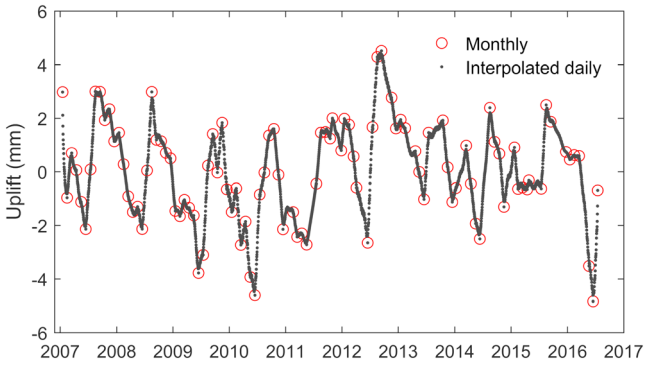

Figure 5. Monthly detrended GRACE-estimated vertical displacements (red circles) and interpolated daily data (gray dots) at SRMP.

previous GPS-based results shown in Figure 4, the eigenvalues corresponding to the first, seventh, and eighth components now lie above the intervals, indicating that the first 10 components are not colored noise but statistically significant signals.

Because of the spectral mixing of transient and seasonal signals in RC 2 as shown in Figures 6 and 7, we reapply M-SSA to the RC 2 components to further separate them and refer to the separated transient and seasonal signals as the decomposed RC 2. Finally, we recover the transient signals and seasonal signals using RCs 1, 3, 4, 5, 6, and the decomposed RC 2. RCs 7 and 8 appear to be seasonal perturbations with small amplitudes and are neglected here.

As shown in Figure 8, the transient and seasonal signals from the three time series are well recovered and show similar temporal variations. At 60 km farther away from the ice, the ice mass loading at UPVK is smaller than that at SRMP. In addition, the semiannual variability is strong at UPVK but relatively weak at SRMP, contributing to the phase difference between the two sites. This could be seen from the comparisons between the GPS and GRACE data at SRMP in Figure 8.

To make the GRACE data comparable with the GPS data, we follow Khan, Wahr, et al. (2010) to apply a correction by multiplying a constant to the GRACE-based uplift. This scaling constant is estimated as 2.04 by fitting the sum of the seasonal and transient signals at SRMP. Then we use this constant to scale up the GRACE-based seasonal and transient signals, respectively. As shown in Figure 9, the scaled GRACE data agree well with the GPS data.

In Figures 8b and 9b, the detected transient signals show an abnormal subsidence (called "Transient Event 1") during mid-2008 and mid-2011 and an abnormal uplift (called "Transient Event 2") during mid-2011 and mid-2014. These anomalies are stronger in GPS signals than in the unscaled GRACE signals (Figure 8b). And the anomalies in GPS signals are stronger at SRMP than at UPVK (Figure 8b). The scaled transient GRACE signals are similar to the GPS signals in both magnitude and phase.

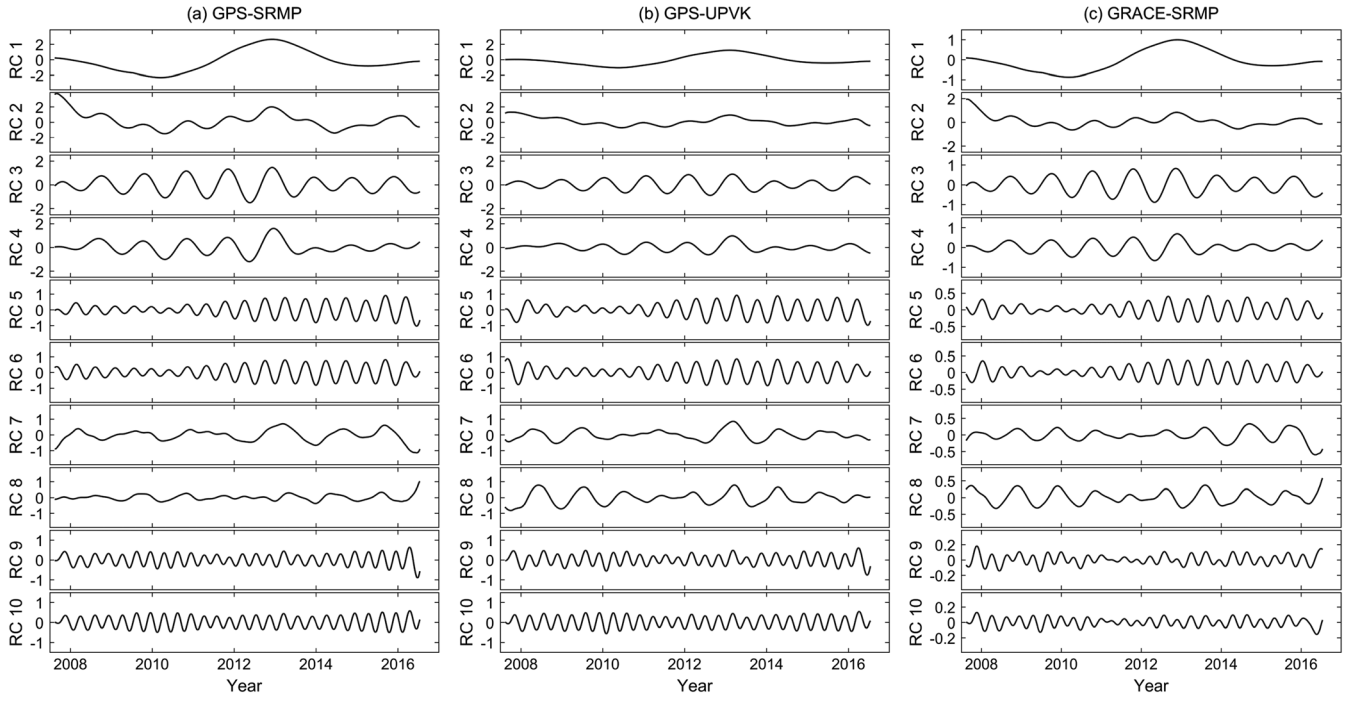

Figure 6. The first 10 reconstructed components (in mm) corresponding to the largest 10 eigenvalues when M-SSA is applied to the daily (a and b) GPS and (c) GRACE data.

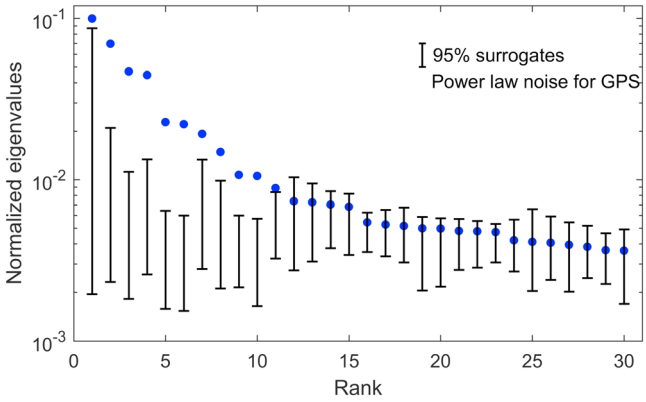

Figure 7. Similar to Figure 4 but for the test results of when MC-SSA is applied to the combined GPS and GRACE data.

6. Forward Modeling of Transient Changes in Ice Mass Loading Displacements

To quantitatively explain the detected transient signals, we investigate the loading displacements due to two glacial mass components, namely, SMB (section 6.1) and glacial dynamics (section 6.2).

6.1. Ice Mass Changes Due To SMB

Using the simulated SMB of Greenland Ice Sheet from the regional climate MAR model (version 3.5.2) forced by European Centre for Medium-Range Weather Forecasts ERA-Interim data (Fettweis et al., 2017), we calculate the radial displacements caused by SMB using the same Green's function method as described in section 3.2. As the SMB output are expressed as monthly increments, we first calculate the accumulated SMB-estimated displacement by integrating the incremental data and then remove a linear trend from it. We refer to the detrended SMB-estimated displacement as the "SMB data" hereafter.

Since there are no "true values" of the SMB fields, we cannot accurately determine the uncertainty of the inferred displacements. Instead, we compare our simulated displacements with those inferred using MAR models forced by two other reanalysis data (NCEP-NCARv1 and 20CRv2) and those from an alternative SMB model Regional Atmospheric Climate Model version 2.3 (Noël et al., 2015). We take the largest difference among these SMB models to give a conservative estimate of the uncertainty in the simulated vertical displacements as ±1.54 mm at SRMP and ±0.87 mm at UPVK. Given the peak-to-peak amplitude of the uplift caused by SMB (~8 mm at SRMP and ~3.8 mm at UPVK), we conclude that the SMB uncertainty has limited influence on the uplift results.

To identify the transient signals in the SMB data, we apply M-SSA to the SMB data at SRMP and UPVK with the same settings as before. Since the monthly SMB data are purely simulation results and do not contain colored noise, the MC-SSA test is unnecessary and thus not performed. Figures 10 shows the reconstructed transient signals at SRMP. The other reconstructed components and seasonal signals are in section S4 in the supporting information. The SMB transient signals showed a very similar varying trend with the GPS and GRACE transient signals during 2011 and 2014. However, the SMB transient signals that occurred during 2008 and 2011 were slightly inconsistent with the GPS and GRACE transient signals during the same period.

6.2. Ice Mass Change Due To Glacial Dynamics

In addition to SMB, changes in ice discharge can also change ice mass balance. There are five marine-terminating outlet glaciers located in UI catchment, losing several to tens of gigatons of ice per year by glacial dynamics (Larsen et al., 2016). To quantify the dynamically induced mass loss and its temporal changes, we perform a simple fluxgate calculation similar to Rignot and Kanagaratnam (2006) and Larsen et al. (2016). We use the glacial surface velocity maps produced by Joughin et al. (2010) and updated in 2017 using synthetic aperture radar (SAR) offset tracking. The time span is from 2009 to 2016, and the temporal interval is about 2.5 months. Figure 11a shows an example of a velocity map for November 2014. We use the ice thickness map constructed by Morlighem et al. (2014). Figure 11a also shows the fluxgates and the glacier catchments we delineate manually based on the spatial patterns of the velocity field and the bedrock elevation map. For simplicity, the mathematical framework described below is for an individual outlet glacier and its catchment.

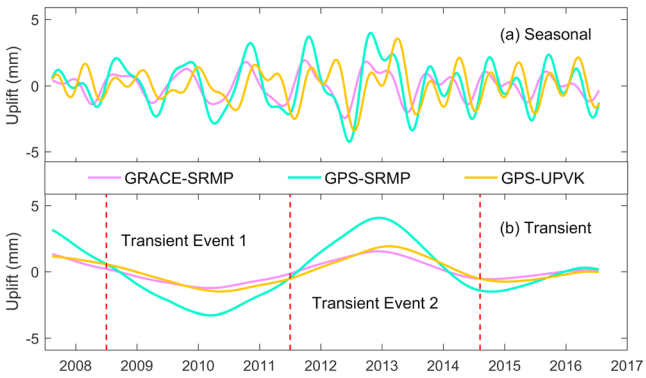

Figure 8. The reconstructed (a) seasonal and (b) transient signals using combined GPS and GRACE data. The red vertical dashed lines indicate the temporal ranges of two detected transient signals.

We follow three steps to calculate the dynamical displacements at the GPS sites. First, we calculate the total ice flux through the fluxgates. Knowing the surface ice velocity V and ice thickness H along a fluxgate with a width W, we calculate the rate of ice mass passing through the fluxgate, denoted as $\dot{m}_D$ by performing the following integral

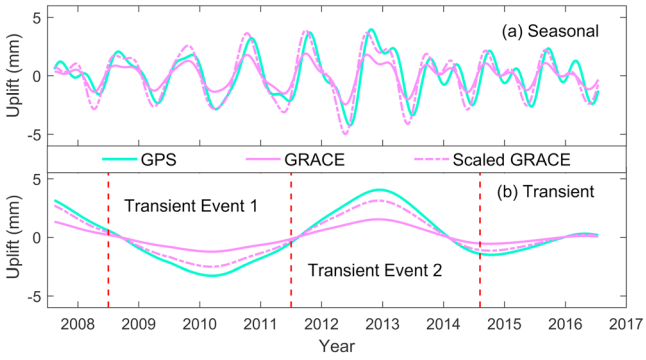

Figure 9. Comparisons among GPS, GRACE, and scaled GRACE data at SRMP. The dashed lines are the scaled GRACE signals generated by multiplying the GRACE data by a constant factor of 2.04.

$$\dot{m}_D(t) = \rho \int_0^W V(t) H dw \tag{11}$$

where ρ is the ice density, set as a constant of 913 kg/m^3 as the study area is located in the ablation zone, and dw is the incremental width. As the fluxgates are set as close to the glacier terminus as possible, the glacier mass losses downstream of the fluxgates are neglected. The only time-varying parameter in equation (11) is the ice velocities. We ignore any temporal change of the ice thickness along the fluxgates.

Figure 12a shows the time series of our calculated dynamic mass loss rates for the five glaciers and their sum. UI-1 showed a moderate mass loss rate before mid-2010, followed by a significant increase, then maintained at a relatively high rate until mid-2011, and then gradually slowed down to the pre-2010 level. UI-2 showed a clear increasing trend in mass loss rate. UI-0, UI-3, and UI-4 showed small and relatively stable mass loss rates from 2009 to 2016.

The surface elastic displacement due to ice dynamics is determined not only by total mass flux change as calculated using equation (11) but also by its spatial distribution within the catchment including retreat of the glacier terminus. So the second step is to distribute the total ice flux within the catchment. We use a simple data-driven approach to distribute the total mass flux. The idea is to estimate the spatial pattern of dynamic mass loss, which is the difference between the total mass loss and the SMB. We use an elevation change map from 2009 to 2014 with a resolution of 2 km, produced using altimetry data from ICESat, IceBridge, and CryoSat-2 (updated from Khan et al., 2013; Kjeldsen et al., 2013; Khan et al., 2016) and take it as the total mass loss. Then we remove the cumulative SMB changes (the MAR outputs) during the same time span from it to obtain ice elevation change induced by glacier dynamics, as shown in Figure 11b. The dynamical ice elevation changes in the drainage basins of UI-0, UI-1, UI-2, and UI-4 are negative values. These are reasonable since dynamic mass loss accounts for ~80% of the total mass loss from the entire UI catchment (Khan et al., 2013; Nielsen et al., 2012). However, the dynamical ice elevation change in the UI-3 basin seems problematic because of many positive values. Nonetheless, the contribution of UI-3 on the dynamical mass changes and the associated vertical loading was small, therefore does not affect our modeled transient uplift much.

We further assume that the dynamic mass loss follows a fixed spatial distribution pattern during any given interval between 2009 and 2016. Namely, we distribute the time-varying total ice flux within the catchment according to constant dynamical elevation changes shown in Figure 11b. We make this strong assumption due to the lack of time-varying ice thickness data. Using this fixed pattern, we can distribute the calculated dynamic mass loss over the ice field for each interval. The sum of the distributed dynamic mass loss within each catchment is equal to the total flux.

After distributing the dynamical mass loss rate, we proceed to the third and final step to use the mass loss rates at all points in Figure 11b to calculate the uplift rates at SRMP and UPVK using the same Green's functions method described in section 3.2. By removing the best fit linear trends from the calculated uplift rates

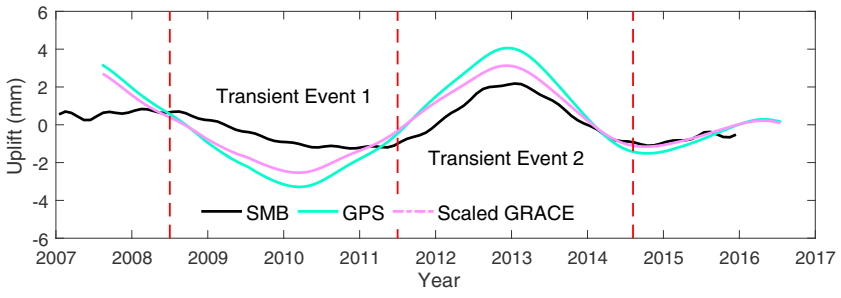

Figure 10. Reconstructed transient signals from GPS, scaled GRACE, and SMB at SRMP. The GPS and scaled GRACE time series are the same as those shown in Figure 9b.

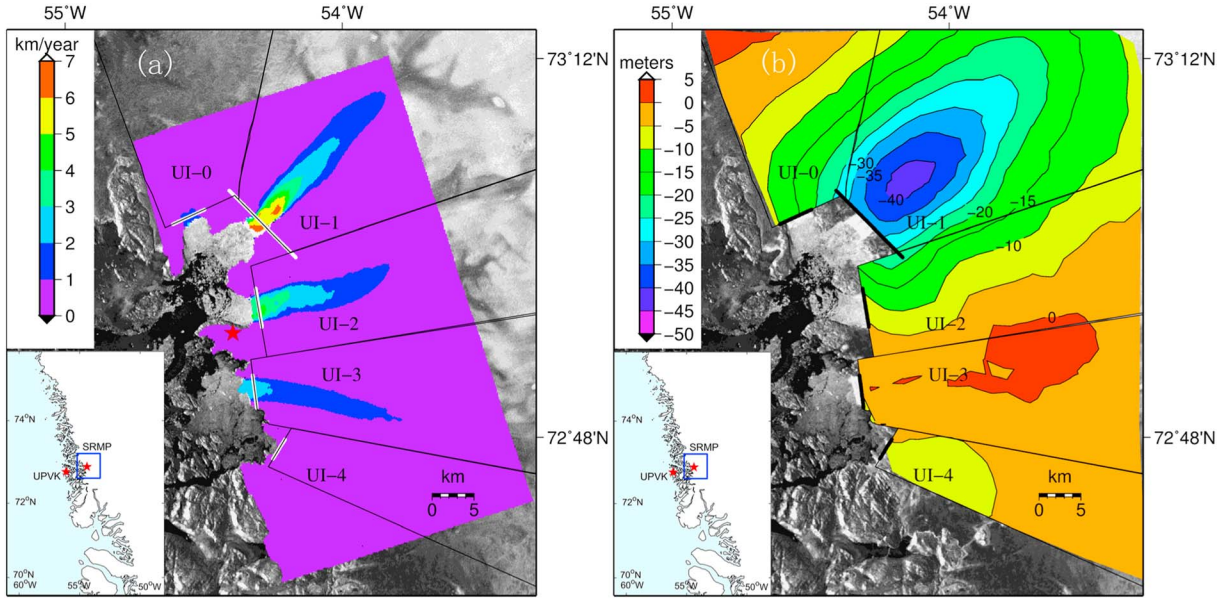

Figure 11. (a) Ice velocity map for Upernavik Isstrøm between 14 November 2014 and 25 November 2014 (based on Joughin et al., 2010, updated in 2017). The white lines mark the fluxgates; the black polygons define drainage basins for each glacier catchment. The red stars indicate the two GPS sites. The inset shows the location of the velocity map in West Greenland. (b) Elevation changes due to dynamical ice mass loss from 2009 to 2014. The background of both maps is a SAR image.

and integrating the residuals, we calculate the transient uplifts referenced to 5 February 2009, that is, the first record of dynamically induced uplift. Figure 12b shows the transient vertical displacements at SRMP caused by individual glacier catchment and their sum. The time series of UI-Sum is characterized by a subsidence before mid-2010 followed by a rapid uplift till late 2011 and then keeping a relatively high position till mid-2014 and then showing a subsidence till mid-2016. Among the five glaciers, UI-1 and UI-2 contributed the most.

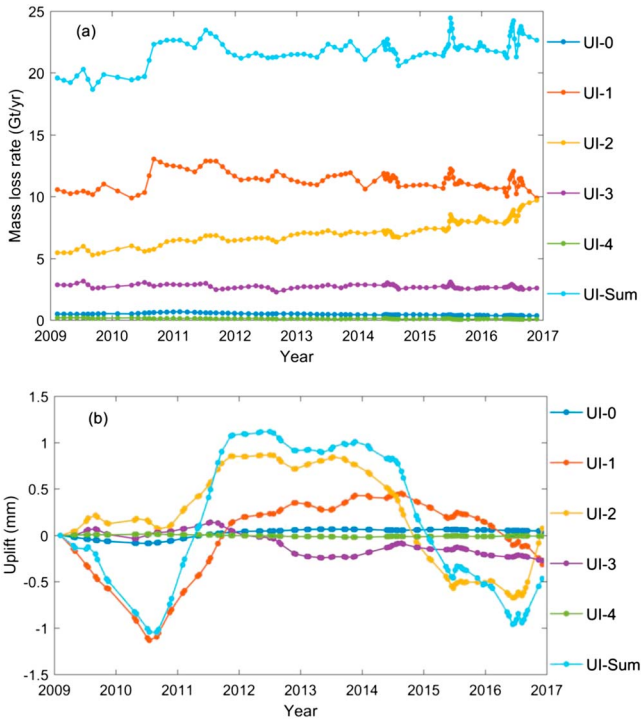

Figure 12. (a) Mass loss rates for the five UI glaciers and their sum. (b) Modeled uplifts at SRMP due to the dynamic ice mass loss from individual glaciers and their sum.

Since the dynamically induced uplift is influenced by complex error sources that are difficult to quantify, we only list three important ones here. First, it is a strong assumption that the dynamical mass change distribution is fixed in time. But in fact, the ice flux divergence, which is directly associated with the distribution of dynamical mass change, is varying with time. Second, the mass loss downstream of the fluxgate is ignored, which may lead to underestimation of the uplift. Third, due to data deficiencies, we assume the ice thickness along the fluxgates to be constant over time. But in fact, the thickness change can be more than 30 m from 2009 to 2014.

7. Discussion

We compare the transient signals inferred from data (GPS and GRACE) and forward models (SMB and glacial dynamics), shown together in Figure 13. The SMB showed very similar varying patterns as the GPS- and GRACE-based time series from mid-2011 to mid-2014, while the glacial dynamics showed only a small uplift during the same period. This indicates that SMB could account for most of the transient signals in GPS and GRACE during this period. The SMB showed a gentle subsidence from mid-2008 to mid-2011, inconsistent with the temporal patterns of the GPS and GRACE data. But enhanced ice discharge also caused a transient subsidence during this period, which had similar temporal patterns as in the GPS and GRACE data, though with a smaller amplitude. This suggests that the subsidence

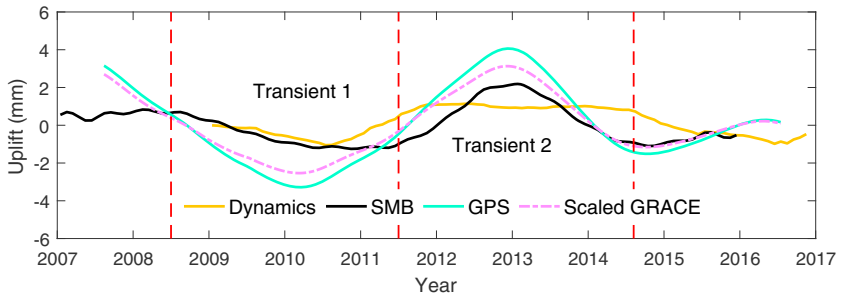

Figure 13. Comparisons among transient signals extracted from GPS, scaled GRACE, SMB, and glacier dynamics at SRMP.

anomalies during this period were due to the combined contributions from both glacial dynamics and SMB.

Overall, our modeled vertical loading displacements due to SMB and glacier dynamics showed some weak synchronization (Figure 13). However, some disagreements can also be observed. For instance, the phases and magnitudes of glacial dynamics were slightly out of phase with the GPS or GRACE data. Since we apply M-SSA to the GPS, GRACE, and SMB data, the smoothing effect may change the phases and amplitudes of GPS signals.

In addition, the colored noise in the GPS time series also affects the amplitudes and phases of the transient signals. In section S2 in the supporting information, we describe our synthetic experiments. We show that in cases of colored noise with large power law index, the chances for misidentifying transient signals as noise are high and it is more difficult to separate transient signals from noise. Another reason for the disagreements is that the temporal resolutions of the velocity fields are low, about five per year. Integrating these discrete velocities over time may introduce some phase shifts. Figure 14 shows the comparisons between the glacier dynamics plus SMB-inferred displacements and the GPS-GRACE-based results. In general, they show a good agreement.

To further investigate the timing and contributors for the transient signals in ice mass change, we calculate the annual mass accumulation and loss from SMB. For any calendar year, we define the accumulation season as from the previous September to May of the given year, and the ablation season as from June to August in the same year. We compute the total mass gain in accumulation seasons and total mass loss in ablation seasons and then convert them to elastic deformations by the Green's functions. The results are shown in Figure 15.

According to this modeling exercise, SRMP uplifted 15.8 mm in the ablation season of 2012, which was significantly larger than the other years. It subsided 6.3 mm in the 2011–2012 accumulation season, which was nearly as much as the other years. This suggests that the uplift anomalies in 2012 were caused by more ablation instead of less-than-normal accumulation. In 2013, the site uplifted approximately by half the amount of the previous year in the ablation season but subsided only ~1 mm more than the previous year, which indicates that the abnormal subsidence in 2013 was mainly due to less-than-normal ablation with minor

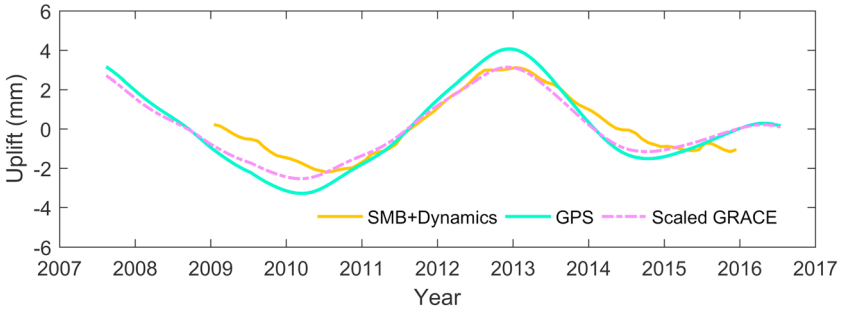

Figure 14. Comparisons between transient signals extracted from GPS, scaled GRACE, and SMB plus glacier dynamics at SRMP.

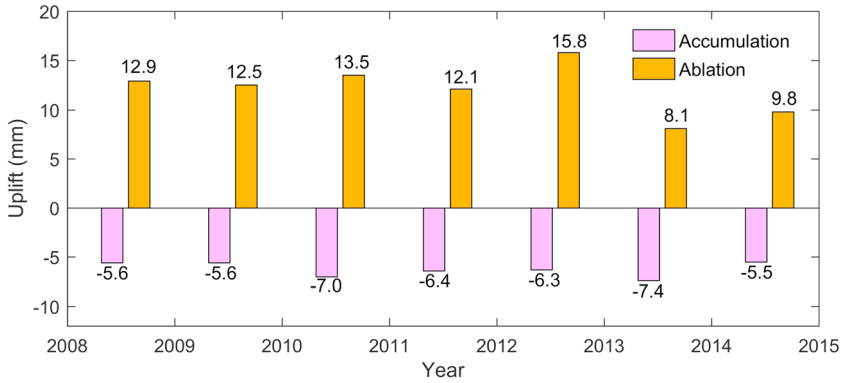

Figure 15. Seasonal cumulative uplifts caused SMB at SRMP. The crustal surface uplifts during ablation seasons from June to August and subsides during accumulation seasons from September to next May.

contributions from more accumulation. For the subsidence in 2009 and uplift in 2010 in GPS and GRACE data, we observe ~1 mm more uplift at SRMP in 2010 ablation season and ~1.4 mm more subsidence in 2009–2010 accumulation season compared with the corresponding values in the previous year. These are too small to explain the large subsidence (~5 mm) in 2009–2010. We, thus, infer that the abnormal variations during this period were mainly caused by glacier dynamics.

8. Conclusions

In this study, we apply M-SSA to the combination of GPS data and GRACE data near Upernavik Isstrøm in West Greenland. We successfully detect two transient anomalies associated with short-term changes in ice mass balance. Our findings and conclusions are as follows. (1) According to our forward models, we find that glacial dynamics and SMB together account for the transient mass gain from mid-2008 to mid-2011, while ablation anomalies account for most of the transient mass loss from 2011 to 2014. (2) When using GPS data alone, transient signals are prone to be identified as colored noise in the MC-SSA test since the presence of transient signals will lead to overestimation of the spectral index and variance of the noise. We demonstrate that adding GRACE data into MC-SSA could suppress this problem to some extent.

This study proves that M-SSA/MC-SSA is a feasible and robust method to study the transient variations in glacial mass. An improved quantification of the short-term variations of glacial mass could help improve the current glacial models.

Acknowledgments

We thank Xavier Fettweis for providing the MAR surface mass balance data, the Center for Space Research (CSR), University of Texas Austin, for providing GRACE data, the UNAVCO Facility for providing GPS data, and the National Snow and Ice Data Center for providing ice flow velocity maps and ice thickness maps. Data generated in this study are available at https://doi.pangaea.de/10.1594/PANGAEA.880159. Work at the Chinese University of Hong Kong was supported by Hong Kong Research Grants Council (CUHK24300414). S. A. K. was funded in part by Carlsbergfondet (grant CF14-0145) and the Danish Council for Independent Research (grant DFF-4181-00126). Raw GPS data are available from the UNAVCO Facility with support from the National Science Foundation (NSF) and National Aeronautics and Space Administration (NASA) under NSF Cooperative Agreement EAR-0735156.

References

Abdalati, W., & Steffen, K. (2001). Greenland Ice Sheet melt extent: 1979–1999. *Journal of Geophysical Research*, *106*(D24), 33,983–33,988. https://doi.org/10.1029/2001JD900181

Adhikari, S., Ivins, E. R., & Larour, E. (2017). Mass transport waves amplified by intense Greenland melt and detected in solid Earth deformation. *Geophysical Research Letters*, *44*, 4965–4975. https://doi.org/10.1002/2017GL073478

Allen, M. R., & Robertson, A. W. (1996). Distinguishing modulated oscillations from coloured noise in multivariate datasets. *Climate Dynamics*, *12*(11), 775–784. https://doi.org/10.1007/s003820050142

Allen, M. R., & Smith, L. A. (1994). Investigating the origins and significance of low-frequency modes of climate variability. *Geophysical Research Letters*, *21*(10), 883–886. https://doi.org/10.1029/94GL00978

Allen, M. R., & Smith, L. A. (1996). Monte Carlo SSA: Detecting irregular oscillations in the presence of colored noise. *Journal of Climate*, *9*(12), 3373–3404. https://doi.org/10.1175/1520-0442(1996)009%3C3373:MCSDIO%3E2.0.CO;2

Altamimi, Z., Métivier, L., & Collilieux, X. (2012). ITRF2008 plate motion model. *Journal of Geophysical Research*, *117*, B07402. https://doi.org/10.1029/2011JB008930

Amiri-Simkooei, A. R. (2013). On the nature of GPS draconitic year periodic pattern in multivariate position time series. *Journal of Geophysical Research: Solid Earth*, *118*, 2500–2511. https://doi.org/10.1002/jgrb.50199

Andresen, C. S., Kjeldsen, K. K., Harden, B., Nørgaard-Pedersen, N., & Kjær, K. H. (2014). Outlet glacier dynamics and bathymetry at Upernavik Isstrøm and Upernavik Isfjord, north-West Greenland. *Geological Survey of Denmark and Greenland Bulletin*, *31*, 79–82.

Bevis, M., Wahr, J., Khan, S. A., Madsen, F. B., Brown, A., Willis, M., … Francis, O. (2012). Bedrock displacements in Greenland manifest ice mass variations, climate cycles and climate change. *Proceedings of the National Academy of Sciences*, *109*, 11,944–11,948. https://doi.org/10.1073/pnas.1204664109

Bos, M. S., Fernandes, R. M. S., Williams, S. D. P., & Bastos, L. (2013). Fast error analysis of continuous GNSS observations with missing data. *Journal of Geodesy*, *87*(4), 351–360. https://doi.org/10.1007/s00190-012-0605-0

Broomhead, D. S., & King, G. P. (1986). Extracting qualitative dynamics from experimental data. *Physica D: Nonlinear Phenomena*, *20*(2-3), 217–236. https://doi.org/10.1016/0167-2789(86)90031-X

Chen, Q., van Dam, T., Sneeuw, N., Collilieux, X., Weigelt, M., & Rebischung, P. (2013). Singular spectrum analysis for modeling seasonal signals from GPS time series. *Journal of Geodynamics*, *72*, 25–35. https://doi.org/10.1016/j.jog.2013.05.005

Cheng, M., Tapley, B. D., & Ries, J. C. (2013). Deceleration in the Earth's oblateness. *Journal of Geophysical Research: Solid Earth*, *118*, 740–747. https://doi.org/10.1002/jgrb.50058

Dettinger, M. D., Ghil, M., Strong, C. M., Weibel, W., & Yiou, P. (1995). Software expedites singular-spectrum analysis of noisy time series. *Eos, Transactions of the American Geophysical Union*, *76*(2), 12–21. https://doi.org/10.1029/EO076i002p00012

Dziewonski, A. M., & Anderson, D. L. (1981). Preliminary reference earth model. *Physics of the Earth and Planetary Interiors*, *25*(4), 297–356. https://doi.org/10.1016/0031-9201(81)90046-7

Fang, M., Dong, D., & Hager, B. H. (2014). Displacements due to surface temperature variation on a uniform elastic sphere with its centre of mass stationary. *Geophysical Journal International*, *196*(1), 194–203. https://doi.org/10.1093/gji/ggt335

Fettweis, X., Box, J. E., Agosta, C., Amory, C., Kittel, C., & Gallée, H. (2017). Reconstructions of the 1900–2015 Greenland ice sheet surface mass balance using the regional climate MAR model. *The Cryosphere*, *11*(2), 1015–1033. https://doi.org/10.5194/tc-11-1015-2017

Fukumori, I. (2002). A partitioned Kalman filter and smoother. *Monthly Weather Review*, *130*(5), 1370–1383. https://doi.org/10.1175/1520-0493(2002)130%3C1370:APKFAS%3E2.0.CO;2

Ghil, M., Allen, M. R., Dettinger, M. D., Ide, K., Kondrashov, D., Mann, M. E., … Yiou, P. (2002). Advanced spectral methods for climatic time series. *Reviews of Geophysics*, *40*, 1003. https://doi.org/10.1029/2000RG000092

Ghil, M., & Vautard, R. (1991). Interdecadal oscillations and the warming trend in global temperature time series. *Nature*, *350*(6316), 324–327. https://doi.org/10.1038/350324a0

Han, D., & Wahr, J. (1995). The viscoelastic relaxation of a realistically stratified earth, and a further analysis of postglacial rebound. *Geophysical Journal International*, *120*(2), 287–311. https://doi.org/10.1111/j.1365-246X.1995.tb01819.x

Hanna, E., Huybrechts, P., Cappelen, J., Steffen, K., Bales, R. C., Burgess, E., … Savas, D. (2011). Greenland ice sheet surface mass balance 1870 to 2010 based on Twentieth Century Reanalysis, and links with global climate forcing. *Journal of Geophysical Research*, *116*, D24121. https://doi.org/10.1029/2011JD016387

Ji, K. H., & Herring, T. A. (2013). A method for detecting transient signals in GPS position time-series: Smoothing and principal component analysis. *Geophysical Journal International*, *193*(1), 171–186. https://doi.org/10.1093/gji/ggt003

Joughin, I., Abdalati, W., & Fahnestock, M. (2004). Large fluctuations in speed on Greenland's Jakobshavn Isbræ glacier. *Nature*, *432*, 608–610. https://doi.org/10.1038/nature03130

Joughin, I., Smith, B., Howat, I., Scambos, T., & Moon, T. (2010). Greenland flow variability from ice-sheet-wide velocity mapping. *Journal of Glaciology*, *56*, 415–430. https://doi.org/10.3189/002214310792447734

Kalnay, E., Kanamitsu, M., Kistler, R., Collins, W., Deaven, D., Gandin, L., … Zhu, Y. (1996). The NCEP/NCAR 40-year reanalysis project. *Bulletin of the American meteorological Society*, *77*(3), 437–471.

Khan, S. A., Kjær, K. H., Bevis, M., Bamber, J. L., Wahr, J., Kjeldsen, K. K., … Muresan, I. S. (2014). Sustained mass loss of the northeast Greenland ice sheet triggered by regional warming. *Nature Climate Change*, *4*(4), 292–299. https://doi.org/10.1038/nclimate2161

Khan, S. A., Kjaer, K. H., Korsgaard, N. J., Wahr, J., Joughin, I. R., Timm, L. H., … Babonis, G. (2013). Recurring dynamically induced thinning during 1985 to 2010 on Upernavik Isstrøm, West Greenland. *Journal of Geophysical Research: Earth Surface*, *118*, 111–121. https://doi.org/10.1029/2012JF002481

Khan, S. A., Liu, L., Wahr, J., Howat, I., Joughin, I., van Dam, T., & Fleming, K. (2010). GPS measurements of crustal uplift near Jakobshavn Isbræ due to glacial ice mass loss. *Journal of Geophysical Research*, *115*, B09405. https://doi.org/10.1029/2010JB007490

Khan, S. A., Sasgen, I., Bevis, M., van Dam, T., Bamber, J. L., Wahr, J., … Munneke, P. K. (2016). Geodetic measurements reveal similarities between post-last glacial maximum and present-day mass loss from the Greenland ice sheet. *Science Advances*, *2*(9), e1600931. https://doi.org/10.1126/sciadv.1600931

Khan, S. A., Wahr, J., Bevis, M., Velicogna, I., & Kendrick, E. (2010). Spread of ice mass loss into northwest Greenland observed by GRACE and GPS. *Geophysical Research Letters*, *37*, L06501. https://doi.org/10.1029/2010GL042460

Kim, S. J., Koh, K., Lustig, M., Boyd, S., & Gorinevsky, D. (2007). An interior-point method for large-scale-regularized least squares. *IEEE Journal of Selected Topics in Signal Processing*, *1*, 606–617. https://doi.org/10.1109/JSTSP.2007.910971

Kjeldsen, K. K., Khan, S. A., Wahr, J., Korsgaard, N. J., Kjær, K. H., Bjørk, A. A., … van Angelen, J. H. (2013). Improved ice loss estimate of the northwestern Greenland ice sheet. *Journal of Geophysical Research: Solid Earth*, *118*, 698–708. https://doi.org/10.1029/2012JB009684

Kondrashov, D., & Ghil, M. (2006). Spatio-temporal filling of missing points in geophysical data sets. *Nonlinear Processes in Geophysics*, *13*, 151–159. https://doi.org/10.5194/npg-13-151-2006

Larsen, S. H., Khan, S. A., Ahlstrøm, A. P., Hvidberg, C. S., Willis, M. J., & Andersen, S. B. (2016). Increased mass loss and asynchronous behavior of marine-terminating outlet glaciers at Upernavik Isstrøm, NW Greenland. *Journal of Geophysical Research: Earth Surface*, *121*, 241–256. https://doi.org/10.1002/2015JF003507

Liu, L., Khan, S. A., van Dam, T., Ma, J. H. Y., & Bevis, M. (2017). Annual variations in GPS-measured vertical displacements near Upernavik Isstrøm (Greenland) and contributions from surface mass loading. *Journal of Geophysical Research: Solid Earth*, *122*, 677–691. https://doi.org/10.1002/2016JB013494

McGuire, J. J., & Segall, P. (2003). Imaging of aseismic fault slip transients recorded by dense geodetic networks. *Geophysical Journal International*, *155*(3), 778–788. https://doi.org/10.1111/j.1365-246X.2003.02022.x

Melachroinos, S. A., Biancale, R., Llubes, M., Perosanz, F., Lyard, F., Vergnolle, M., … Durand, S. (2008). Ocean tide loading (OTL) displacements from global and local grids: Comparisons to GPS estimates over the shelf of Brittany, France. *Journal of Geodesy*, *82*, 357–371. https://doi.org/10.1007/s00190-007-0185-6

Moon, T., Joughin, I., Smith, B., & Howat, I. (2012). 21st-century evolution of Greenland outlet glacier velocities. *Science*, *336*, 576–578. https://doi.org/10.1126/science.1219985

Morlighem, M., Rignot, E., Mouginot, J., Seroussi, H., & Larour, E. (2014). Deeply incised submarine glacial valleys beneath the Greenland ice sheet. *Nature Geoscience*, *7*(6), 418–422. https://doi.org/10.1038/ngeo2167

Nielsen, K., Khan, S. A., Korsgaard, N. J., Kjær, K. H., Wahr, J., Bevis, M., … Timm, L. H. (2012). Crustal uplift due to ice mass variability on Upernavik Isstrøm, west Greenland. *Earth and Planetary Science Letters*, *353*, 182–189.

Noël, B., Van De Berg, W. J., Van Meijgaard, E., Kuipers Munneke, P., Van De Wal, R. S. W., & Van De Broeke, M. R. (2015). Evaluation of the updated regional climate model RACMO2. 3: Summer snowfall impact on the Greenland ice sheet. *The Cryosphere*, *9*(5), 1831–1844. https://doi.org/10.5194/tc-9-1831-2015

Ohtani, R., McGuire, J. J., & Segall, P. (2010). Network strain filter: A new tool for monitoring and detecting transient deformation signals in GPS arrays. *Journal of Geophysical Research*, *115*, B12418. https://doi.org/10.1029/2010JB007442

Penna, N. T., & Stewart, M. P. (2003). Aliased tidal signatures in continuous GPS height time series. *Geophysical Research Letters*, *30*(23), 2184. https://doi.org/10.1029/2003GL018828

Petrov, L., & Boy, J. P. (2004). Atmospheric pressure loading for routine data analysis. *arXiv preprint physics/0401117*.

Rangelova, E., Sideris, M. G., & Kim, J. W. (2012). On the capabilities of the multi-channel singular spectrum method for extracting the main periodic and non-periodic variability from weekly GRACE data. *Journal of Geodynamics*, *54*, 64–78. https://doi.org/10.1016/j.jog.2011.10.006

Rangelova, E., Van der Wal, W., Sideris, M. G., & Wu, P. (2010). Spatiotemporal analysis of the GRACE-derived mass variations in North America by means of multi-channel singular spectrum analysis. In *Gravity, Geoid and Earth Observation* (pp. 539–546). Berlin: Springer. https://doi.org/10.1007/978-3-642-10634-7_72

Ray, J., Altamimi, Z., Collilieux, X., & van Dam, T. (2008). Anomalous harmonics in the spectra of GPS position estimates. *GPS Solutions*, *12*, 55–64. https://doi.org/10.1007/s10291-007-0067-7

Riel, B., Simons, M., Agram, P., & Zhan, Z. (2014). Detecting transient signals in geodetic time series using sparse estimation techniques. *Journal of Geophysical Research: Solid Earth*, *119*, 5140–5160. https://doi.org/10.1002/2014JB011077

Rignot, E., & Kanagaratnam, P. (2006). Changes in the velocity structure of the Greenland ice sheet. *Science*, *311*(5763), 986–990. https://doi.org/10.1126/science.1121381

Rodell, M., Houser, P. R., Jambor, U. E. A., Gottschalck, J., Mitchell, K., Meng, C. J., … Toll, D. (2004). The global land data assimilation system. *Bulletin of the American Meteorological Society*, *85*, 381–394. https://doi.org/10.1175/BAMS-85-3-381

Steffen, K., & Box, J. (2001). Surface climatology of the Greenland ice sheet: Greenland climate network 1995–1999. *Journal of Geophysical Research*, *106*(D24), 33,951–33,964. https://doi.org/10.1029/2001JD900161

Swenson, S., Chambers, D., & Wahr, J. (2008). Estimating geocenter variations from a combination of GRACE and ocean model output. *Journal of Geophysical Research*, *113*, B08410. https://doi.org/10.1029/2007JB005338

Tedesco, M., Fettweis, X., Mote, T., Wahr, J., Alexander, P., Box, J. E., & Wouters, B. (2013). Evidence and analysis of 2012 Greenland records from spaceborne observations, a regional climate model and reanalysis data. *The Cryosphere*, *7*(2), 615–630. https://doi.org/10.5194/tc-7-615-2013

Theiler, J., Eubank, S., Longtin, A., Galdrikian, B., & Farmer, J. D. (1992). Testing for nonlinearity in time series: The method of surrogate data. *Physica D: Nonlinear Phenomena*, *58*(1-4), 77–94. https://doi.org/10.1016/0167-2789(92)90102-S

Tregoning, P., & van Dam, T. (2005). Atmospheric pressure loading corrections applied to GPS data at the observation level. *Geophysical Research Letters*, *32*, L22310. https://doi.org/10.1029/2005GL024104

van Dam, T., Wahr, J., & Lavallée, D. (2007). A comparison of annual vertical crustal displacements from GPS and Gravity Recovery and Climate Experiment (GRACE) over Europe. *Journal of Geophysical Research*, *112*, B03404. https://doi.org/10.1029/2006JB004335

van Dam, T., Wahr, J., Milly, P. C. D., Shmakin, A. B., Blewitt, G., Lavallée, D., & Larson, K. M. (2001). Crustal displacements due to continental water loading. *Geophysical Research Letters*, *28*(4), 651–654. https://doi.org/10.1029/2000GL012120

van Dam, T. M., & Wahr, J. M. (1987). Displacements of the Earth's surface due to atmospheric loading: Effects on gravity and baseline measurements. *Journal of Geophysical Research*, *92*(B2), 1281–1286. https://doi.org/10.1029/JB092iB02p01281

Vautard, R., & Ghil, M. (1989). Singular spectrum analysis in nonlinear dynamics, with applications to paleoclimatic time series. *Physica D: Nonlinear Phenomena*, *35*(3), 395–424.

Vautard, R., Yiou, P., & Ghil, M. (1992). Singular-spectrum analysis: A toolkit for short, noisy chaotic signals. *Physica D: Nonlinear Phenomena*, *58*(1-4), 95–126. https://doi.org/10.1016/0167-2789(92)90103-T

Wahr, J., Khan, S. A., van Dam, T., Liu, L., Angelen, J. H., Broeke, M. R., & Meertens, C. M. (2013). The use of GPS horizontals for loading studies, with applications to northern California and southeast Greenland. *Journal of Geophysical Research: Solid Earth*, *118*, 1795–1806. https://doi.org/10.1002/jgrb.50104

Walwer, D., Calais, E., & Ghil, M. (2016). Data-adaptive detection of transient deformation in geodetic networks. *Journal of Geophysical Research: Solid Earth*, *121*, 2129–2152. https://doi.org/10.1002/2015JB012424

Williams, S. D., Bock, Y., Fang, P., Jamason, P., Nikolaidis, R. M., Prawirodirdjo, L., … Johnson, D. J. (2004). Error analysis of continuous GPS position time series. *Journal of Geophysical Research*, *109*, B03412. https://doi.org/10.1029/2003JB002741

Williams, S. D. P. (2003). The effect of coloured noise on the uncertainties of rates estimated from geodetic time series. *Journal of Geodesy*, *76*(9-10), 483–494. https://doi.org/10.1007/s00190-002-0283-4

Williams, S. D. P., & Penna, N. T. (2011). Non-tidal ocean loading effects on geodetic GPS heights. *Geophysical Research Letters*, *38*, L09314. https://doi.org/10.1029/2011GL046940